inorganics

MDPI

Article

Multistimuli Luminescence and Anthelmintic Activity of Zn(II) Complexes Based on 1H-Benzimidazole-2-yl Hydrazone Ligands

Alexey Gusev [1], Elena Braga [1], Alexandr Kaleukh [1], Michail Baevsky [1], Mikhail Kiskin [2] and Wolfgang Linert [3,*]

[1] General Chemistry Department, Crimean Federal University V.I. Vernadsky, Simferopol 295007, Russia; galex0330@gmail.com (A.G.); braga.yelena@ya.ru (E.B.); alexander.kaleukh@yandex.ru (A.K.); b_m_y@mail.ru (M.B.)
[2] Kurnakov Institute of General and Inorganic Chemistry, Russian Academy of Sciences, Moscow 119991, Russia; m_kiskin@mail.ru
[3] Institute of Applied Physics, Vienna University of Technology, Wiedner Hauptstraße 8-10, 1040 Vienna, Austria
* Correspondence: wolfgang.linert@tuwien.ac.at; Tel.: +43-1-58801-163613

Abstract: Three novel Zn(II) mononuclear complexes with the general formula ZnL_2Cl_2 (L = 2-(4-R-phenylmethylene)benzimidazol-2-hydrazines; R-H (1), R-CH_3 (2), and R-OCH_3 (3)) were synthesized and fully characterized by various means. These complexes demonstrate excitation-dependent emission, which is detected by a change in the emission color (from blue to green) upon an increase in the excitation wavelength. Moreover complex 1 shows reversible mechanochromic luminescence behavior due to the reversible loss of solvated methanol molecules upon the intense grinding of crystals. In addition, 1 exhibits vapochromic properties, which originate from the adsorption methanol vapor on the crystal surface. The strengthening of anthelmintic activity at the transition from free hydrazones to zinc-based complexes is shown.

Keywords: benzimidazoles; hydrazones; zinc(II) complexes; photoluminescence; biological activity

Citation: Gusev, A.; Braga, E.; Kaleukh, A.; Baevsky, M.; Kiskin, M.; Linert, W. Multistimuli Luminescence and Anthelmintic Activity of Zn(II) Complexes Based on 1H-Benzimidazole-2-yl Hydrazone Ligands. *Inorganics* **2024**, *12*, 256. https://doi.org/10.3390/inorganics12090256

Academic Editor: Santo Di Bella

Received: 24 August 2024
Revised: 14 September 2024
Accepted: 18 September 2024
Published: 23 September 2024

1. Introduction

Mechano-/vapochromic luminescent materials have been actively researched in the past few decades because such compounds possess great potential for applications in different promising fields such as information security, chemosensors, and optical data storage devices [1–3]. In particular, mechanochromic luminescence displays a reversible color change in emission triggered by grinding, compressing, shearing, and other mechanical stimulus. Most reported mechanochromic materials are created for organic compounds and to a lesser extent for transition metal complexes containing Cu(I), Pt(II), Au(I/III), Ir(III) [4–11], and much less Zn [12–14] ions.

Significant interest in mechanoluminescent materials is related to the possibility of changing the optical response of the system without the chemical bond's cleavage. Indeed, the origin of the mechanochromism and reversible color change arises from either a change in the molecular conformation, the molecular arrangements, or a transformation in the crystalline packing features: hydrogen bonds, $\pi-\pi$ stacking, and van der Waals forces. Certain relationships between mechano-/vapochromic luminescent behavior and molecular arrangements before and after mechanical stimulation and several general design approaches to create mechano-/vapochromic luminescent materials have been described in several reviews [1,2,4]. Despite significant advances in the creation of mechanochromic materials, the targeted synthesis of such compounds is an unresolved challenge and requires expanding the number of objects with such properties.

Benzimidazole derivatives are well-known organic ligands used to construct luminescent coordination compounds with various metal ions. The combination of the properties of

imidazole derivatives with the nature of the luminescence imposed by different metals is important for the development of new functional materials [15–17] and catalysators [18]. Some of the organic molecules containing benzimidazole core demonstrate mechanochromic luminescence while metal-organic complexes are quite rare.

Herein, we present the design and synthesis of a new Schiff base (L1–L3) and its zinc(II) complexes (ZnL_2Cl_2) through the self-assembly 2-(4-R-phenylmethylene)benzimidazol-2-hydrazines (Scheme 1). and zinc ion. We expected that the extended chain of π-bonds and the possibility of different coordination modes of L would create prerequisites for the realization of molecular packing features, changes in which would change the luminescent signal. Moreover, benzimidazole derivatives are a promising core of many pharmaceutical drugs, which allows us to consider complexes based on them as a direction of search for new biologically active compounds [19,20].

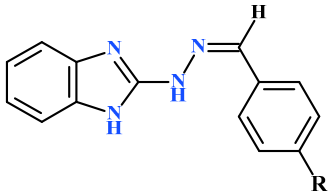

R - H (L^1), CH_3 (L^2), CH_3O (L^3)

Scheme 1. Ligands L1–L3 used in this study.

2. Results

2.1. General Characterization of Complexes

Benzimidazole derivatives L1 and L2 were synthesized according to modified methods [20]. Zn complexes 1–3, as greyish-green crystalline solids, were isolated by refluxing zinc chloride with 2-(4-R-phenylmethylene)benzimidazol-2-hydrazines (L1–L3) in a 1:1 molar ratio in methanol and were further purified by recrystallization from a suitable solvent. All the products are stable in solution and in the solid state upon extended exposure to air. Complexes 1–3 were fully characterized by elemental analysis, infrared, and electronic absorption spectroscopy. The elemental analysis data of the Zn(II) complexes agree well with the theoretical composition. Phase purities were confirmed by the powder XRD. The molar conductance values in the methanol solution (10^{-4} M) suggest the complexes 1–3 are non-electrolytes.

Analysis of the IR spectra of the zinc complexes (Figures S1–S3) indicate that most of the peaks are almost similar to that of the spectrum of the uncoordinated ligands except for minor shifts in the position of some of the peaks. Characteristic vibrations of the azomethine bond are non-shifted upon complex formation, while characteristic in-plane and out-of-plane deformation bands of the imidazole rings shift to higher frequencies in comparison with similar free ligands, indicating of the coordination of the ligand through the imidazole nitrogen atoms with the monodentate coordination mode.

Given the possibility of chelate ring formation during complex formation, the monodentate method of coordination seems thermodynamically disadvantageous. Therefore, the monodentate coordination of the ligand should be compensated by the energy gain due to the packing features in the crystal (Scheme 2).

Thermal analyses (Figure S4) showed the expected increase in the decomposition temperature of the complexes compared to the free ligands. The TGA curve of complex 1 shows that complex thermally decomposed in two steps. The first weight loss of 3.6% is in the 108–147 °C range, which is associated with the removal of lattice methanol (calc. 5%). The following step, from 273 °C, corresponds to the decomposition of the organic part of complex 1.

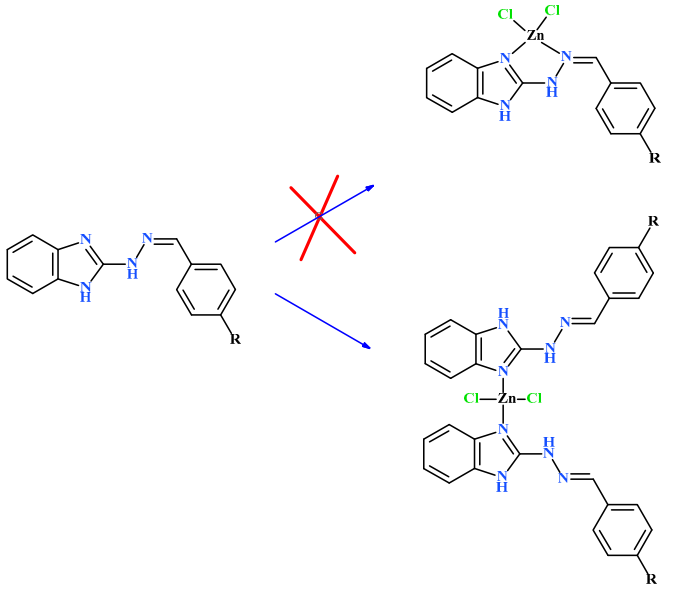

Scheme 2. Synthesis of the Zn complexes with L1–L3.

Complex 3 is stable up to a temperature of 169 °C, above which the process of desolvation starts, gradually proceeding to the decomposition of the compound. Complex 2 demonstrates maximum thermal stability. Noticeable loss of mass begins at temperatures above 230 °C with the process of removal of solvate molecules DMSO proceeding together with the decomposition of the complexes.

Well-shaped single crystals of 1–3 were obtained from the recrystallization of the complex in methanol, DMF, and DMSO, respectively. Crystallographic data and refinement parameters of the structures are summarized in Table S1. Complex 1 crystallizes in the monoclinic space group $P2_1/c$, while complexes 2 and 3 crystallize in the triclinic space group $P\bar{1}$. In all cases, zinc cation coordinated to two nitrogen atoms from distinct benzimidazole ring ligands and two chloride ligands, assuming almost ideal tetrahedral geometry (τ_4 (1) = 0.97; τ_4 (2) = 0.98; τ_4 (3) = 0.95) [21]. The coordination bond lengths ranged from 1.985(2) Å to 2.2823(6) Å and angles from 105.35(4)° to 115.9(1)°. Coordination bond lengths and angles are summarized in Table S2. 1H-benzimidazole-2-yl hydrazine molecules are almost planar; maximal deviation of these atoms from the best-fit mean plane through them, 0.166 Å (1), 0.215 Å (2), 0.180 Å (3). The dihedral angles between the benzimidazole ring and phenyl ring in the complexes of 1, 2, and 3 are in the range of 4.51–7.94°, 6.56°–10.11°, and 9.38°–11.53°, respectively.

Further analysis of the crystalline structure of 1 shows that the independent units are linked through N3-H3···Cl1, N6-H6···Cl1, N7-H7···Cl2, O1S-H1S···Cl2, and N2-H2···O1S hydrogen bond interactions to generate a two-dimensional structure. Except for the hydrogen bond interactions, the intermolecular π···π stacking interactions play important roles in assembling the 2D structures. As shown in Figure 1, a 2D layer is additionally constructed by interlayer $\pi_{imid}\cdots\pi_{imid}$ (3.289 Å) stacking interactions.

Supramolecular arrangements of 2 and 3 in crystals are slightly different (Figures S2 and S3). Single crystal analysis of 2 reveals that adjacent molecules are linked by N-H···Cl hydrogen bond interactions to form a supramolecular dimer. Mononuclear units of complex 3 are interconnected through intermolecular hydrogen bonds involving neighboring complex and solvate DMF and water molecules.

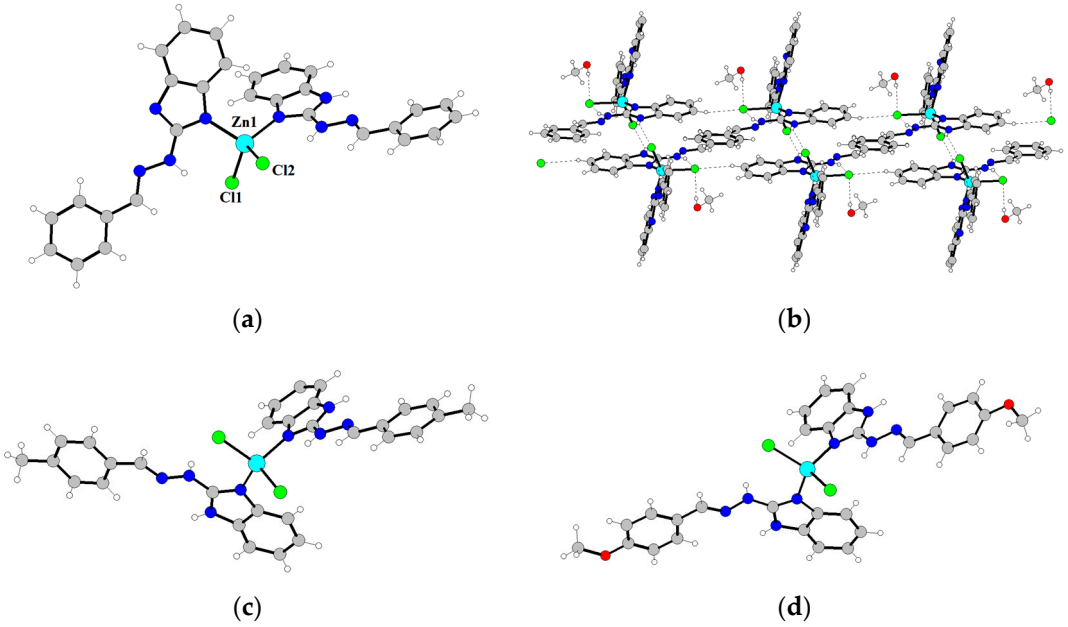

Figure 1. Crystal and molecular structures of 1 (**a**), 2 (**c**), and 3 (**d**). Solvate molecules are omitted for clarity. Fragment of supramolecular architecture of 1 (**b**) (Colour of the atoms: grey—C; red—O; green—Cl; blue—Zn; deep blue—N).

2.2. Photophysical Properties of Zinc Complexes

Electronic absorption spectra were recorded for solid state samples at room temperature. Figure S4 shows the absorption spectra of title complexes. It is found that all the complexes exhibit two absorption bands at ca. 260–266 nm (as a shoulder) and ca. 336–354 nm. These absorption bands are similar to the corresponding ligands, which can be assigned to the π–π* and n–π* transitions of the ligands. Beside this, UV-Vis spectra contain broad signals centered at 700 nm. The more probable source of this band is associated with exciton transitions that arise from interactions between the complex molecules in the π-stacks.

Upon irradiation by a UV lamp, dried air crystals of complex 1 demonstrate strong greenish-blue luminescence. The emission spectra of the as-prepared crystals of 1 exhibit intense unstructured bands with the maxima at 517 nm upon excitation at 410 nm (maximum at excitation spectra) with CIE coordinates at (0.23:0.49). Quantum yield determined in these conditions reached 19.2%.

Further investigations demonstrated that under a UV lamp, the ground samples show a bluer luminescence than follows from the instrumental measurements of CIE-coordinates at 410 nm excitation. This prompted us to investigate the luminescence spectra upon excitation at different wavelengths. Detailed studies of luminescent properties of complex 1 exhibit obvious excitation-dependent emissions [22]. Upon step-by-step changing of the excitation wavelength from 410 to 425 nm, the intensity of the emission band gradually decreases, and the maximum is slightly shifted from 517 to 525 nm. Upon excitation at lower wavelengths (375–405 nm), the complex demonstrates a dual emission band with the maxima around 505 and 440 nm. At the same time, there is a distinct tendency, as the excitation wavelength decreases, the intensity of the long-wavelength band gradually decreases, while the short-wavelength maximum becomes dominant. Visually, the shift in the luminescence spectrum of a crystalline sample upon excitation shifting is perceived as a change in the emission color from greenish blue to deep blue.

Grinding the crystals in an agate mortar leads to a decrease in the luminescence intensity (quantum yield is 13.8%) and to a shift of the luminescence maximum to the long-wave region to 538 nm (λ_{ex} = 430 nm) with a change of the color emission to blueish green (CIE coordinates 0.32:0.61). It should be noted that the effect of the dependence of the

emission maximum on the excitation wavelength is practically not observed for crushed crystals. So, when ground crystals are excited with a wavelength of 365 nm, the emission maximum is registered at 526 nm.

The lifetimes of 1 before and after grinding were determined from the decay profiles by fitting the double-exponential decay curves.

$$y = A1\exp(-x/\tau 1) + A2\exp(-x/\tau 2)$$

For the initial crystals of **1** (Figure S5), luminescence at 517 nm decays were approximated, with the following parameters: $\tau 1 = 4.61$ ns, $\tau 2 = 14.12$ ns with comparable contributions by both components that indicate there are at least two deactivation channels of the excited state. The decay of emission at 538 nm of the grounded crystals of **1** are approximated by the monoexponential function ($\tau = 13.26$ ns).

Deep insight into the observed phenomena powder X-ray diffraction (PXRD) analysis of the ground sample of **1** are provided (Figure S5). After grinding, the PXRD pattern intensity became weak and broad, but in general, the crystal structure of the complex is preserved upon grinding. These results indicate that the mechano-responsive properties of **1** should not be attributed to the phase transitions of the crystalline samples to amorphous states. In our opinion, the origin of the dual luminescence of complex **1** is the superposition of the solvated (signal at 407–430 nm) and unsolvated complex forms (signal at 505–510 nm). Observed emission changes may be related to the partial loss of the methanol solvate molecule during intensive crystal grinding. Indeed, thermogravimetric analysis of 1 after grinding shows weight loss values of methanol are 1.8%, indicating that part of the methanol was lost upon grinding.

To further confirm this hypothesis, crystals of complex **1** were vacuum dried at 100 °C to constant mass. Elemental analysis of the dried crystals showed the absence of solvate methanol molecules in the complex. The luminescence spectrum of the dried sample of complex **1** was completely identical to that of the crushed complex and contained one maximum at 538 nm. The detected solvochromism of complex **1** prompted us to investigate the properties of complex **1** when exposed to methanol vapor. Vapor-stimuli experiments were conducted by putting the sample in an airtight container, which was full of the saturated methanol vapor. The luminescent spectral investigations show that the sample exposed to MeOH demonstrates intense blue photoluminescence (λ_{max} = 407 nm CIE coordinates (0.18; 0.25)) when excited by a 375 nm wavelength (Figure 2b). It is noteworthy that the sample incubated in methanol vapor also exhibits excitation-dependent emission, but in this case, the signal at 407 nm with an emission efficiency of 15.4% is dominant in intensity. Further mechanical treatment in an agate mortar or drying in air of a sample soaked in methanol vapor leads to the recovery of the long-wavelength signal and the appearance of green luminescence (Figure 2c,d).

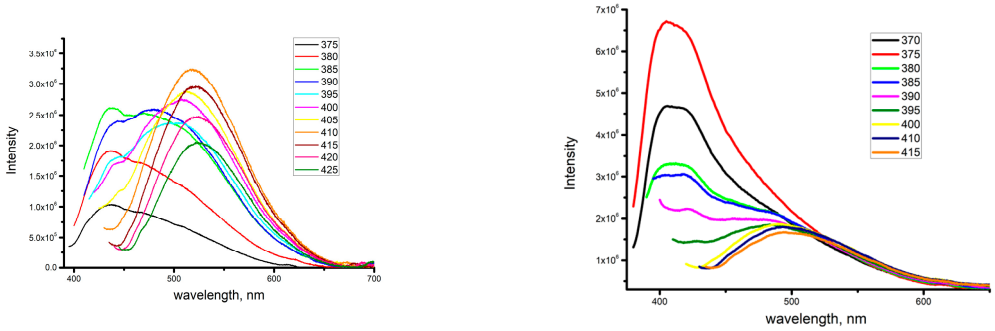

(**a**) (**b**)

Figure 2. *Cont.*

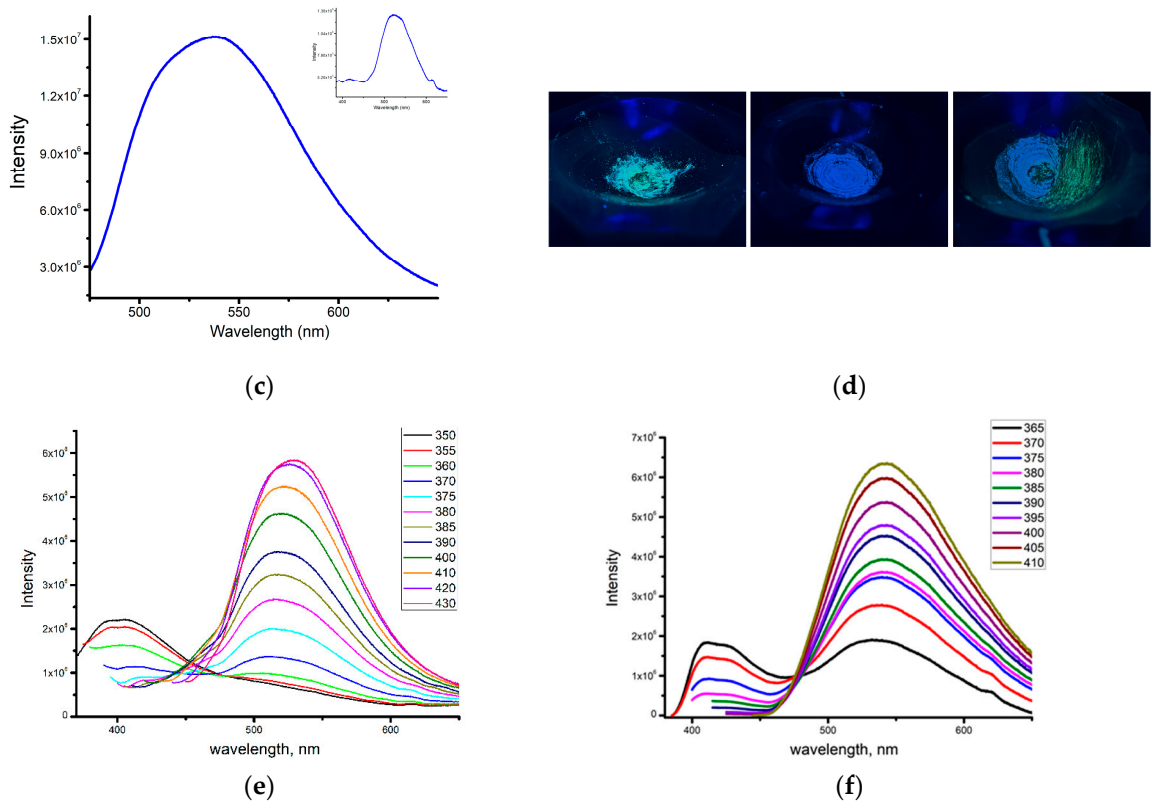

Figure 2. (**a**) Emission spectra of as-prepared crystals of 1 at different excitation. (**b**) Emission spectra of 1 after treatment of CH_3OH vapor at different excitation. (**c**) Emission spectra of 1 after grinding (exc. at 430 nm) (inset emission excited at 365 nm). (**d**) Image of as-prepared crystals after treatment and after grinding under UV lamp. (**e**) Emission spectra of as-prepared crystals of 2 at different excitation. (**f**) Emission spectra of as-prepared crystals of 3 at different excitation.

Single crystals of 2 and 3 also demonstrate excitation-dependent behavior. At the excitation at 355 nm, the as-prepared crystals of complexes **2** and **3** show weak blue emission with the emission bands centered at 406 and 411 nm with fluorescence quantum yields of 1.8% and 1.1%, respectively. Further studies show that the emission maxima of **2** change from 406 nm to 543 nm gradually upon increasing the excitation wavelengths from 355 to 430 nm. As a result, the emission colors turned from blue to greenish yellow (Figure 2e,f). The emission at 543 nm displays the strongest intensity upon excitation at 430 with (QY 9.8%). Similar behavior was demonstrated with complex 3, for which the emission maximum shifted from 411 to 532 nm when the wavelength changed from 355 to 420 nm, while the quantum yield of 3 reached 6.8%. Interestingly, in contrast to **1,** single crystals of 2 and 3 do not exhibit mechano-/vapocromic properties. A possible reason for this could be the low volatility of the DMF and DMSO solvate molecules.

2.3. Theoretical Studies

In order to obtain better insight into the origin of the emission properties of the studied complexes, DFT and TD-DFT calculations were performed. Figures 1 and 2 show the optimized geometries and HOMO/LUMO orbital patterns of all complexes, respectively. Simulated absorption and fluorescence characteristics in both gas and solvent phases are collected in Table 1. The ground-state optimized geometries of all Zn(II) complexes confirm the planer ligand structure. Multiple ligand rotations around the Zn atom in each of the complexes are possible in various optimized structural conformations at the global minima of the potential energy surface. We thus obtained two types of optimized structures of each complex: one with a parallel ligand alignment and one with a perpendicular ligand orientation. The N-Zn-N and Cl-Zn-Cl angles for the parallel ligand-ligand orientation are

89° and 126°, respectively (Figure 3), while for the perpendicular orientation, these angles were found to be 99° and 121°, respectively.

Table 1. Computed parameters of absorption and emission spectra of 1–3.

	Gaseous Phase		Methanol	
Gaseous Phase	**Methanol**	**λ_{fl} (nm)**	**λ_{abs} (nm)**	**λ_{fl} (nm)**
1	346 (f = 0.595)	539 (f = 0.03)	345 (f = 0.937)	457 (f = 0.136)
2	346 (f = 0.73)	527 (f = 0.04)	345 (f = 1.12)	437 (f = 1.037)
3	345 (f = 0.90)	525 (f = 0.05)	345 (f = 1.35)	440 (f = 0.154)

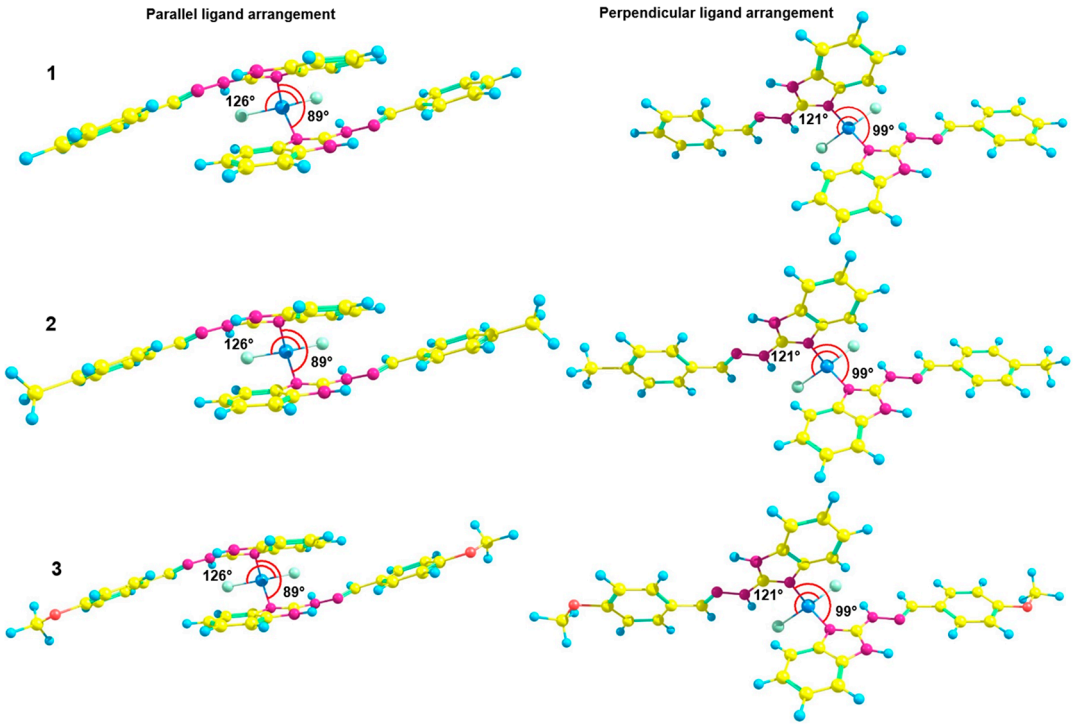

Figure 3. Optimized geometries of chemical structures of complexes 1–3.

The mutual ligand orientation significantly affects their photophysical properties. We have found that all the complexes prefer the strong π-stacking between the two ligands at the S0 and S1 state optimized geometries, while perpendicular ligand arrangement of the complex molecule is not maintained during S1 state optimization regardless of the S0 state geometry arrangement. This may be attributed to the absence of crystal constraints around the complex molecule during a single molecule optimization at the S1 state. From the experimental analysis of the crystalline structures, it is clear that the perpendicular ligand arrangement of an individual unit is maintained in a single crystal structure due to intermolecular hydrogen-bond interactions. Due to the absence of intermolecular hydrogen bonds and π. . .π stackings during a single molecule optimization at the S1 state, the intra-ligand interactions might be the possible reason for the parallel ligand arrangement in the complex state. When the perpendicular torsional angle coordinate between two ligands of the same complex molecule (like in S0 state optimized geometry) was kept frozen during S1 state optimization, the ligand structure was distorted, leading to the twisted charge transfer state within the single ligand. Thus, we speculate that in the real crystal phase, the perpendicular arrangement of the complex both in the S0 and S1 states is stabilized by the surrounding crystal as well as the planar structure of the ligands. We thus assume that the complex model with the parallel ligand alignment is a good model for studying the solid-state luminescence of studied complexes because the planar ligand structure is unchanged in the S1 state, excitation is always localized on one particular ligand, and

Zn ions do not contribute to the S1 excitation. Based on these findings, we computed the absorption and fluorescence spectra of all complexes using the structures with the parallel ligand-ligand stacking characteristic. The photophysical properties of this conformation show a good agreement with the experimental results for all compounds.

The frontier molecular orbitals corresponding to the S1 state configuration for all complexes are localized on 2-(4-R-phenylmethylene)benzimidazol-2-hydrazines ligands (Figure 4). It confirms that the ligands are solely responsible for the absorption and emission properties of the complexes, while Zn atoms plays the role of complexing centers that makes system more stable and rigid, i.e., favorable for fluorescence by suppressing non-radiative processes. The HOMO functions are considerably delocalized over the whole ligand, while the LUMO is localized predominantly on the edge phenyl groups of the ligand.

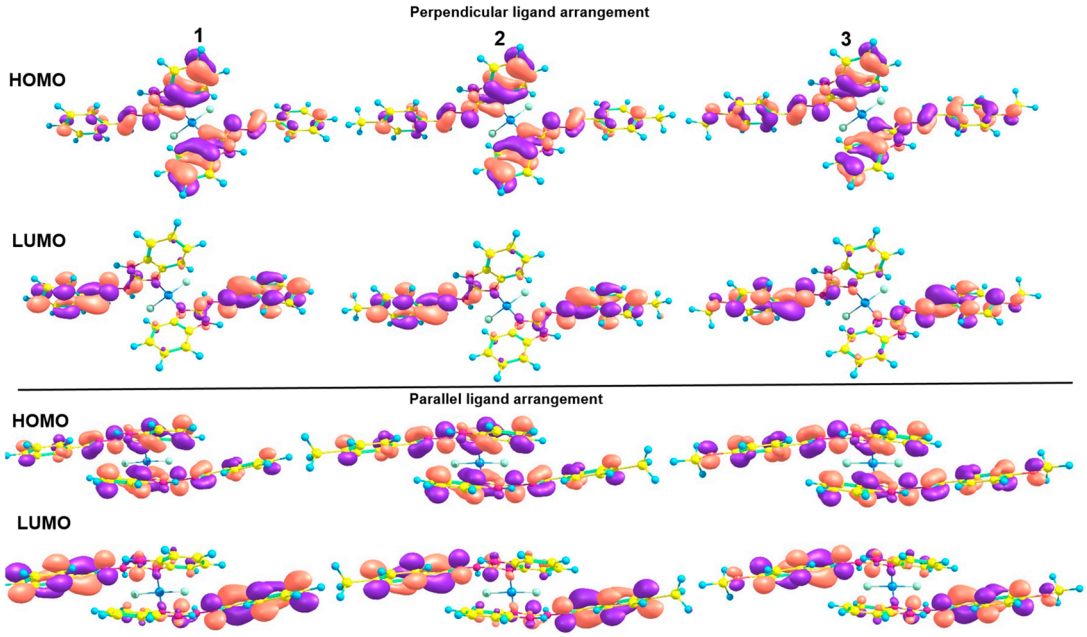

Figure 4. HOMO and LUMO orbitals of all molecules. *(pink and purple colours means positive and negative sign of wave function).*

The absorption and emission maxima computed in a gas phase are in good agreement with the experimental spectra of the crystalline complexes (Table 1). The values of absorption maxima in the gas phase of 1, 2, and 3 are 346, 346, and 345 nm with high oscillator strength values, respectively. These absorption peaks can be assigned to the π–π* transition within the ligand. The corresponding values for fluorescence are 539, 527, and 525 nm. To reproduce the absorption and emission spectra of the crystalline complexes treated with methanol, we computed both properties in the solvent phase with methanol as the solvent model. The values are given in Table 1, which are in line with the experimental fluorescence maxima of the crystalline complexes treated with methanol. Indeed, our calculations confirm the blue shift of the fluorescence, together with growing its intensity in the presence of methanol, compared to the state without the solvent effect.

2.4. Antiparasitic Activities

The anthelmintic activity of hydrazone compounds L1–L3 and the zinc(II) complexes based on them were studied in vitro. The results obtained by the biological assay are given in Table 2.

Table 2. Anthelmintic activity of hydrazone compounds L1–L3 and zinc(II) complexes.

Compounds	24 h		48 h	
	Dicrocoelium Lanceatum	Fasciola Hepatica	Dicrocoelium Lanceatum	Fasciola Hepatica
L1	54	61	78	69
1	86	94	100	96
L2	48	55	54	57
2	69	62	84	64
L3	20	9	27	16
3	51	16	58	35
Albendazole	29	21	32	27
Triclabendazole	68	47	72	58
$ZnCl_2$	-	-	-	-

As can be seen from the presented data, hydrazones and complexes based on them show appreciable anthelmintic activity against Dicrocoelium lanceatum and Fasciola hepatica. Earlier, the work of M. A. Argirova and co-authors showed that similar L1–L3 compounds also exhibit high anthelmintic activity, the effect of which depends on the type and position of the substituent in the aldehyde fragment [20]. In the L1–L3 series, the substituent also plays a prominent role. Specifically, the anthelmintic activity of L1–L3 compounds decreases in the 4-H, 4-CH_3, 4-CH_3O series, amounting to 78, 54, and 27% for Dicrocoelium lanceatum and 69, 57, and 16% for Fasciola hepatica, respectively. The activity of L1 is comparable with the traditional drugs Albendazole and Triclabendazole. An interesting fact is the enhancement of anthelmintic activity of hydrazones in coordination with zinc cation. In all cases, the activity increases 1.5–2 times, and in the case of complex 1, it reaches 100% efficacy. This fact can play a significant role in the development of new anthelmintic drugs.

3. Materials and Methods

All the reagents and solvents were commercially available and used as received without further purification. 1H-benzimidazole-2-yl hydrazones were prepared according to the literature method [20].

Elemental analyses of C, H, and N were performed with the EuroEA 3000 analyzer. The IR spectra were measured by the FSM 2202 spectrometer in the range of 4000–400 cm^{-1}. Diffuse reflection spectra were recorded with a Cintra-3000 spectrophotometer for the solid-state samples. Photoluminescence and excitation spectra were recorded on the Fluorolog FL3-22 spectrometer for the complexes in solid state. Luminescence decays were measured using the same spectrometer equipped with a xenon flash lamp. The luminescence quantum yields of the solid samples were determined by the absolute method using an integrating sphere. The thermal behavior of complexes 1–3 was studied using the simultaneous thermal analysis (STA) technique.

3.1. Synthetic Procedures

Related ligands (L1–L3) 2 mmol and $ZnCl_2$ (137 mg, 1 mmol) were dissolved in 40 mL and 10 mL CH_3OH, respectively, and then these two solutions were mixed together. After stirring for about 2 h at 60 °C, the reaction mixture was cooled, and crude complexes were collected by filtration. Pure crystalline samples were obtained by recrystallization of crude products from MeOH (1), DMF (2), and DMSO (3), respectively.

$Zn(L1)_2 \cdot CH_3OH$ (**1**) Yield 27%. Anal. calc. (%) for $C_{29}H_{27}Cl_2N_8OZn$: C, 54.43; H, 4.25; N, 17.51. Found (%): C, 54.62; H, 4.32; N, 17.75. IR (cm^{-1}): 3279 w, 3198 w, 3054 w, 1638 s, 1616 m 1592 s, 1532 s, 1467 s, 1423 m, 1371 m, 1345 m, 1276 m, 1230 m, 1131 m, 1045 s, 935 m, 737 s, 688 s, 619 m, 552 s, 499 s, 461 s, 432 m.

$Zn(L2)_2 \cdot DMSO$ (**2**) Yield 23%. Anal. calc. (%) for $C_{32}H_{34}Cl_2N_8OSZn$: C, 53.75; H, 4.79; N, 15.67. Found (%): C, 53.37; H, 4.59; N, 15.44. IR (cm^{-1}): 3287 w, 3189 w, 3060 w, 1630 s,

1610 m 1591 s, 1527 s, 1466 s, 1424 m, 1371 m, 1345 m, 1275 m, 1235 m, 1121 m, 1106 m, 1054 s, 923 m, 816 s, 736 s, 639 s, 541 s, 516 s, 493 m, 437 m.

$Zn(L3)_2 \cdot DMF$ (**3**) Yield 34%. Anal. calc. (%) for $C_{33}H_{35}Cl_2N_9O_3Zn$: C, 53.42; H, 4.75; N, 16.99. Found (%): C, 53.16; H, 4.60; N, 17.12. IR (cm^{-1}): 3265 w, 3202 w, 3063 w, 1634 s, 1612 m 1593 s, 1530 s, 1464 s, 1423 m, 1370 m, 1303 m, 1249 m, 1169 m, 1105 s, 1031 m, 829 m, 740 s, 656 m, 530 s, 502 m, 461 s, 428 m.

The single crystal X-ray diffraction data for 1–3 were collected using the Bruker APEX II diffractometer equipped with a CCD detector and a graphite-monochromated MoKα radiation source (λ = 0.71073 Å). The structures of complexes were solved by the direct methods and refined in the full-matrix anisotropic approximation for all non-hydrogen atoms. The hydrogen atoms of water molecules were found in differential Fourier maps, and their parameters were refined using the riding model. The hydrogen atoms of the carbon-containing ligand were positioned geometrically and refined by using a riding model. All the calculations were performed by direct methods using the SHELX–2014 and OLEX-2 program package [23,24]. The crystallographic parameters and the structure refinement statistics for 1–3 are shown in Table S1.

3.2. Computational Details

The density functional theory (DFT) and time-dependent (TD) DFT calculations were accomplished with Gaussian 16 software [25]. The ground-state optimization calculations were carried out using the B3LYP functional [26,27] and 6–31G(d) basis set [28]. The same basis set with TD-DFT and B3LYP functionals were employed to calculate vertical absorption spectra and to optimize the first excited singlet state (S1) responsible for fluorescence behavior. The ground and excited state calculations were performed in the gas phase approximation at the first stage. Additionally, the excited-state calculations were also carried out by using Polarizable Continuum Model (PCM)5 of solvent (methanol was used as a model solvent). The Grimme's dispersion correction was accounted for during S0 and S1 states optimization at the GD3 level. No imaginary frequencies were found for any of the optimized structures [29,30].

3.3. Anthelmintic Activity Research

The initial hydrazones and complexes based on them were tested for anthelmintic activity against Dicrocoelium lanceatum and Fasciola hepatica larvae provided from the collection of the Crimean Federal University.

Freshly decapsulated larvae of the above parasites (100 specimens per 1 mL of physiological solution) were exposed to rastovor compounds dissolved in dimethyl sulfoxide (DMSO) (100 μg/mL) and incubated at 37 °C. Albendazole and Triclabendazole was used as standard anthelmintics. After 24 and 48 h, larval viability was determined by fluorescence microscopy. The efficacy (%) of 1H-benzimidazol-2-yl hydrazones and complexes based on them on the viability of Dicrocoelium lanceatum and Fasciola hepatica was calculated as the average of three experiments, according to the formula.

$$\text{Anthelmintic efficacy} = (\text{Number of larvae dead}/\text{original number of larvae}) \times 100\%$$

4. Conclusions

In summary, three different solvates of zinc complexes with 1H-benzimidazole-2-yl hydrazones were synthesized and characterized by standard techniques, including the crystal structure. Crystal structure determination has shown that title complexes have molecular structures with tetracoordinated zinc cation. The extended H-bonds network and π···π stacking interactions between adjacent complex and solvent molecules give rise to a 2D supramolecular architecture. Fluorescent properties studied in the solid state have revealed that the photoluminescence demonstrate excitation-dependent properties. Moreover, Zn(II) complex 1 exhibits a fluorescence color change from blue to green under high grinding. The relationship between the structure and mechanochromic luminescence property of

the Zn(II) complex has been investigated in detail experimentally and theoretically. It was shown that mechanochromism is caused by desolvation of samples during their grinding. The anthelmintic activity of both initial ligands and complexes based on them was also analyzed. It was shown that coordination with zinc cation leads to a marked enhancement of antiparasitic activity.

Supplementary Materials: The following supporting information can be downloaded at: https://www.mdpi.com/article/10.3390/inorganics12090256/s1, Table S1: Crystal data and structure refinements for the complexes **1**–**3**; Table S2: Selected bond's lengths and angles of complexes **103**; Figure S1: TG curve of **1**–**3**; Figure S2: Crystal packing for complex **2**; Figure S3: Crystal packing for complex **3**; Figure S4: UV-vis spectra of solid samples of **1**–**3**; Figure S5: PXRD patterns of for ground and crystalline sample of complex **1**.

Author Contributions: Conceptualization, A.G.; methodology, E.B. and A.K.; validation, W.L. and A.G.; formal analysis, E.B. and A.K.; investigation, M.B., M.K., E.B. and A.K.; writing—original draft preparation, A.G.; writing—review and editing, M.K. and W.L.; supervision, A.G. and W.L.; project administration W.L. All authors have read and agreed to the published version of the manuscript.

Funding: This research received no external funding.

Data Availability Statement: The original contributions presented in the study are included in the article/Supplementary Material, further inquiries can be directed to the corresponding author.

Acknowledgments: M. Kiskin thanks the state assignment of the IGIC RAS in the field of fundamental scientific research for the possibility to perform X-ray diffraction analyses.

Conflicts of Interest: The authors declare no conflicts of interest.

References

1. Hirai, Y. On Sense and Deform: Molecular Luminescence for Mechanoscience. *ACS Appl. Opt. Mater.* **2024**, *2*, 1025–1045. [CrossRef]
2. Sagara, Y.; Yamane, S.; Mitani, M.; Weder, C.; Kato, T. Mechanoresponsive Luminescent Molecular Assemblies: An Emerging Class of Materials. *Adv. Mater.* **2016**, *28*, 1073. [CrossRef] [PubMed]
3. Ma, Z.; Wang, Z.; Teng, M.; Xu, Z.; Jia, X. Mechanically Induced Multicolor Change of Luminescent Materials. *ChemPhysChem* **2015**, *16*, 1811. [CrossRef] [PubMed]
4. Wang, X.-Y.; Lv, L.; Sun, L.; Hou, Y.; Hou, Z.; Chen, Z. Recent Advances in Mechanochromism of Metal-Organic Compounds. *Front. Chem.* **2022**, *10*, 865198. [CrossRef] [PubMed]
5. Kobayashi, A.; Kato, M. Stimuli-responsive Luminescent Copper(I) Complexes for Intelligent Emissive Devices. *Chem. Lett.* **2017**, *46*, 154. [CrossRef]
6. Jin, M.; Ito, H. Solid-state luminescence of Au(I) complexes with external stimuli-responsive properties. *J. Photochem. Photobiol. C Photochem. Rev.* **2022**, *51*, 100478. [CrossRef]
7. López-de-Luzuriaga, J.M.; Monge, M.; Olmos, M.E. Luminescent aryl–group eleven metal complexes. *Dalton Trans.* **2017**, *46*, 2046. [CrossRef]
8. Gusev, A.; Kiskin, M.; Braga, E.; Zamnius, E.; Kryukova, M.; Karaush-Karmazin, N.; Baryshnikov, G.; Minaev, B.; Linert, W. Structure and emission properties of dinuclear copper(I) complexes with pyridyltriazole. *RSC Adv.* **2023**, *13*, 3899. [CrossRef] [PubMed]
9. Peñuelas, C.A.; Campos-Gaxiola, J.J.; Soto-Rojo, R.; Cruz-Enríquez, A.; Reynoso-Soto, E.A.; Miranda-Soto, V.; García, J.J.; Flores-Álamo, M.; Baldenebro-López, J.; Glossman-Mitnik, D. Synthesis of a New Dinuclear Cu(I) Complex with a Triazine Ligand and Diphenylphosphine Methane: X-ray Structure, Optical Properties, DFT Calculations, and Application in DSSCs. *Inorganics* **2023**, *11*, 379. [CrossRef]
10. Malakhova, J.A.; Berezin, A.S.; Glebov, E.M.; Sannikova, V.A.; Vorob'ev, A.Y.; Pervukhina, N.V.; Naumov, D.Y.; Kolybalov, D.S.; Syrokvashin, M.M.; Vinogradova, K.A. Luminescent polymorphism of mononuclear Cu(I) complexes with pyrazolo [1,5-a][1,10]phenanthrolines. *Inorganica Chim. Acta* **2023**, *555*, 121604. [CrossRef]
11. Girish, Y.; Prashantha, K.; Byrappa, K. Recent advances in aggregation-induced emission of mechanochromic luminescent organic materials. *Emergent Mater.* **2021**, *4*, 673–724. [CrossRef]
12. Zheng, H.-W.; Wu, M.; Yang, D.-D.; Liang, Q.-F.; Li, J.-B.; Zheng, X.-J. Multistimuli Responsive Solid-State Emission of a Zinc(II) Complex with Multicolour Switching. *Inorg. Chem.* **2021**, *60*, 11609–11615. [CrossRef]
13. Li, S.; Wu, M.; Kang, Y.; Zheng, H.W.; Zheng, X.J.; Fang, D.C.; Jin, L.P. Grinding-Triggered Single Crystal-to-Single Crystal Transformation of a Zinc(II) Complex: Mechanochromic Luminescence and Aggregation-Induced Emission Properties. *Inorg. Chem.* **2019**, *58*, 4626–4633. [CrossRef]

14. Wang, D.; Shao, T.-F.; Li, S.-M.; Cao, W.; Yao, Q.; Ma, Y. A triphenylamine derivative with multistimuli responsive behavior and high-contrast vapochromism of its Zn(II) complex. *Dye. Pigment.* **2024**, *226*, 112114. [CrossRef]
15. Li, J.-B.; Zheng, H.-W.; Wu, M.; Liang, Q.-F.; Yang, D.-D.; Zheng, X.-J. Mechanochromic Luminescence of Four Zn(II)/Cd(II) Complexes Based on Same Schiff-base Ligand with Different Coordination Modes. *Cryst. Growth Des.* **2021**, *21*, 6937–6946. [CrossRef]
16. Zhang, G.; Xia, X.; Xu, J.; Xia, L.; Wang, C.; Wu, H. A zinc(II) coordination polymer based on a flexible bis(benzimidazole) ligand: Synthesis, crystal structure and fluorescence study. *Z. Naturforsch.* **2020**, *75*, 1005–1009. [CrossRef]
17. Temerova, D.; Kisel, K.S.; Eskelinen, T.; Melnikov, A.S.; Kinnunen, N.; Hirva, P.; Shakirova, J.R.; Tunik, S.P.; Grachova, E.V.; Koshevoy, I.O. Diversifying the luminescence of phenanthro-diimine ligands in zinc complexes. *Inorg. Chem. Front.* **2021**, *8*, 2549. [CrossRef]
18. Milani, J.L.S.; Oliveira, I.S.; Dos Santos, P.A.; Valdo, A.K.S.M.; Martins, F.T.; Cangussu, D.; Das Chagas, R.P. Chemical fixation of carbon dioxide to cyclic carbonates catalyzed by zinc(II) complex bearing 1,2-disubstituted benzimidazole ligand. *Chin. J. Catal.* **2018**, *39*, 245. [CrossRef]
19. Anichina, K.; Mavrova, A.; Vuchev, D.; Popova-Daskalova, G.; Bassi, G.; Rossi, A.; Montesi, M.; Panseri, S.; Fratev, F.; Naydenova, E. Benzimidazoles Containing Piperazine Skeleton at C-2 Position as Promising Tubulin Modulators with Anthelmintic and Antineoplastic Activity. *Pharmaceuticals* **2023**, *16*, 1518. [CrossRef]
20. Argirova, M.A.; Georgieva, M.K.; Hristova-Avakumova, N.G.; Vuchev, D.I.; Popova-Daskalova, G.V.; Anichina, K.K.; Yancheva, D.Y. New 1H-benzimidazole-2-yl hydrazones with combined antiparasitic and antioxidant activity. *RSC Adv.* **2021**, *11*, 39848–39868. [CrossRef]
21. Yang, L.; Powell, D.R.; Houser, R.P. Structural variation in copper(I) complexes with pyridylmethylamide ligands: Structural analysis with a new four-coordinate geometry index, τ4. *Dalton Trans.* **2007**, *9*, 955–964. [CrossRef] [PubMed]
22. Gusev, A.; Braga, E.; Zamnius, E.; Kiskin, M.; Kryukova, M.; Baryshnikova, A.; Minaev, B.; Baryshnikov, G.; Ågren, H.; Linert, W. Structure and excitation-dependent emission of novel zinc complexes with pyridyltriazoles. *RSC Adv.* **2019**, *9*, 22143–22152. [CrossRef] [PubMed]
23. Sheldrick, G.M. SHELXT–Integrated space-group and crystal-structure determination. *Acta Crystallogr. Sect. A Found Adv.* **2015**, *71*, 3–8. [CrossRef]
24. Dolomanov, O.V.; Bourhis, L.J.; Gildea, R.J.; Howard, J.A.; Puschmann, H. OLEX2: A complete structure solution, refinement and analysis program. *J. Appl. Crystallogr.* **2009**, *42*, 339–341. [CrossRef]
25. Frisch, M.J.; Trucks, G.W.; Schlegel, H.B.; Scuseria, G.E.; Robb, M.A.; Cheeseman, J.R.; Scalmani, G.; Barone, V.; Mennucci, B.; Petersson, G.A.; et al. *Gaussian 16*; Revision C.01; Gaussian, Inc.: Wallingford, CT, USA, 2019.
26. Becke, A.D. Density-functional exchange-energy approximation with correct asymptotic behavior. *Phys. Rev. A* **1988**, *38*, 3098. [CrossRef]
27. Becke, A.D. Density-Functional Thermochemistry. III. The Role of Exact Exchange. *J. Chem. Phys.* **1993**, *98*, 5648–5652. [CrossRef]
28. Díaz-Tinoco, M.; Romero, J.; Ortiz, J.V.; Reyes, A.; Flores-Moreno, R. A generalized any-particle propagator theory: Prediction of proton affinities and acidity properties with the proton propagator. *J. Chem. Phys.* **2013**, *138*, 194108. [CrossRef]
29. Tomasi, J.; Mennucci, B.; Cammi, R. Quantum mechanical continuum solvation models. *Chem. Rev.* **2005**, *105*, 2999–3094. [CrossRef]
30. Grimme, S.; Antony, J.; Ehrlich, S.; Krieg, H. A consistent and accurate ab initio parametrization of density functional dispersion correction (DFT-D) for the 94 elements H-Pu. *J. Chem. Phys.* **2010**, *132*, 154104. [CrossRef]